Materials Today • Volume xxx, Number xx • xxxx 2023 RESEARCH

ELSEVIER

Fully enclosed microbeads structured TENG arrays for omnidirectional wind energy harvesting with a portable galloping oscillator

RESEARCH: Original Research

Leo N.Y. Cao [a,b,1], Erming Su [a,b,1], Zijie Xu [a,b,1], Zhong Lin Wang [a,b,c,d,*]

[a] Beijing Institute of Nanoenergy and Nanosystems, Chinese Academy of Sciences, Beijing 100083, China
[b] School of Nanoscience and Technology, University of Chinese Academy of Sciences, Beijing 100049, China
[c] School of Materials Science and Engineering, Georgia Institute of Technology, Atlanta, GA 30332-0245, USA
[d] Yonsei Frontier Lab, Yonsei University, Seoul 03722, Republic of Korea

To facilitate the transition of triboelectric nanogenerators (TENG) from early stages to large-scale real-world applications, urgent mass production is imperative, necessitating standardized manufacturing processes. In this study, a novel "pause-and-insert" and "print-in-place" 3D printing approach has been devised, employing widely available fused deposition modeling (FDM) printers along with conductive (as electrodes) and nonconductive (for casing and support) filaments to make encapsulate microbeads triboelectric nanogenerator (MB-TENG). This innovation results in a fully enclosed freestanding-mode TENG pack, seamlessly integrated with a lightweight wind-induced oscillator featuring tuning systems, thus enabling efficient, safe, and noiseless omnidirectional wind energy harvesting. Through adept design and manufacturing techniques, systematic inner-structure optimization has been achieved, yielding superior output and industrialization levels compared to similar efforts. MB-TENG's surface charge density is as high as 19.9 $\mu C/m^2$. The average power density is 13.8 W/m^3. Moreover, the elimination of postprocessing significantly streamlines standard manufacturing, enhancing the prospects for device commercialization. Beyond its wind energy application, the versatile energy packs can serve as both ocean wave and human motion harvesters within network configurations, capable of powering a massive real-time monitoring sensor array.

Keywords: Triboelectric nanogenerator; Microbeads; Omnidirectional wind oscillator; Distributed network; 3D printing

Introduction

In the era of the internet of things (IoT) combined with artificial intelligence (AI), the integration of vast numbers of IoT devices, particularly sensors, serves as the cornerstone of the fourth industrial revolution [1,2]. These devices play a crucial role by supplying substantial amounts of essential data, enabling us to address critical global challenges such as energy scarcity, population growth, and food shortages [3]. Consequently, there is a growing need for these devices to have access to energy sources that are not only affordable and adaptable but also possess long-lasting and distributed characteristics.

To address this demand, the triboelectric nanogenerator (TENG), invented by Zhong Lin Wang's research group in 2012, proves to be an exceptional solution [4,5]. Serving as a valuable supplement to traditional green energy alternatives [6–8], the TENG technology showcases unique characteristics, such as self-powered functionality, cost-effectiveness, adaptability, and a wide range of material options [5,9–13]. Operating through a combination of triboelectrification and electrostatic induction, the TENG technology is governed by Maxwell's displacement current in its underlying physics model [14]. By lever-

* Corresponding author.
E-mail address: Wang, Z.L. (zhong.wang@mse.gatech.edu)
[1] These authors contributed equally to this work.

 https://doi.org/10.1016/j.mattod.2023.11.001

Please cite this article in press as: L.N.Y. Cao et al., Materials Today (2023), https://doi.org/10.1016/j.mattod.2023.11.001

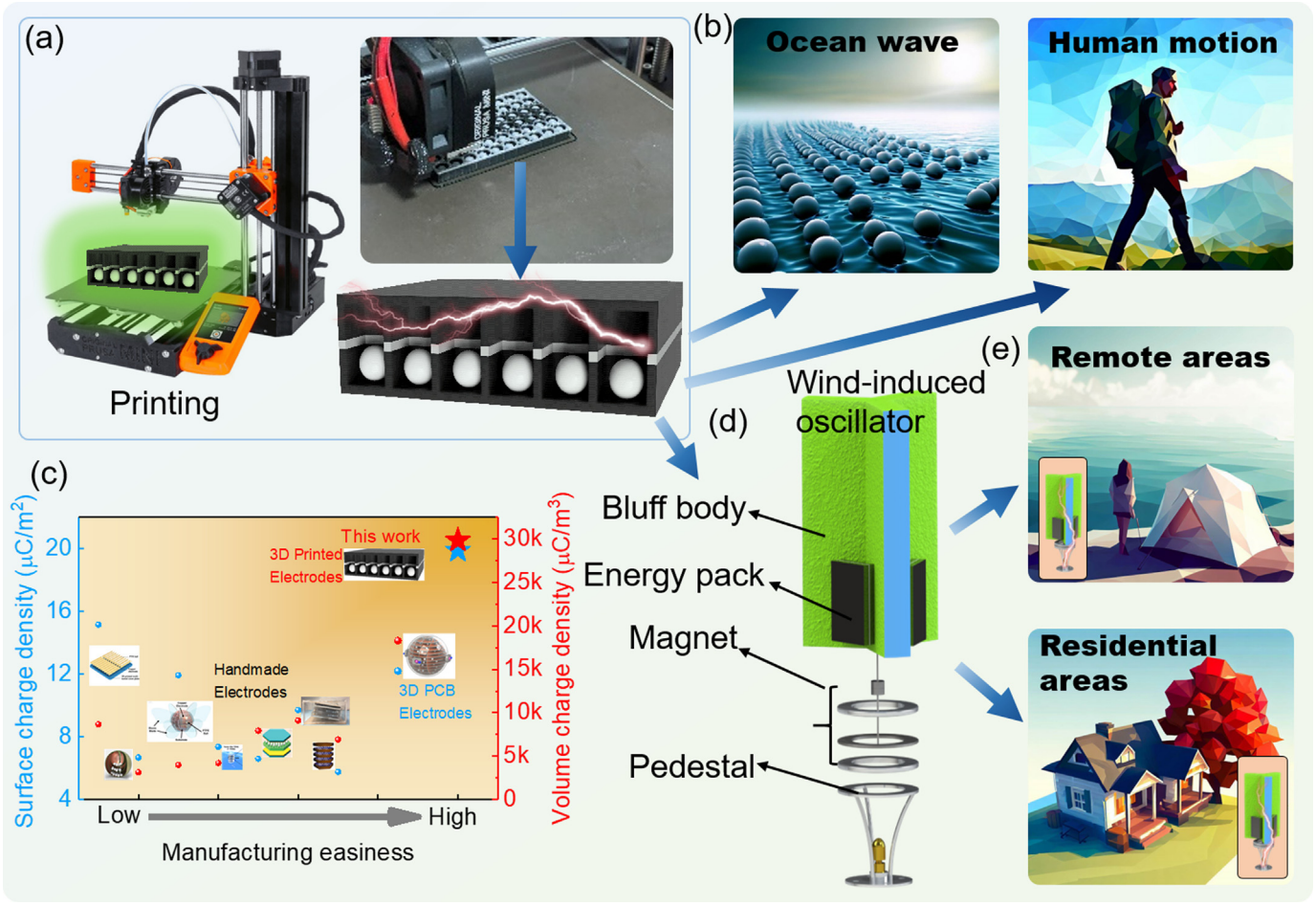

FIG. 1

Structural design and application prospects of the TENG pack. (a) Schematic diagram of the manufacturing. (b) The energy pack application scenario. (c) Comparison of the charge density and manufacturing easiness of this work with other works. (d) MB-TENG schematic diagram. (e) Prospect of MB-TENG application scenario.

aging these principles, the TENG technology offers promising prospects for powering IoT devices efficiently and sustainably.

However, in order to facilitate the transition of TENG from its early stage to large-scale real-world applications, there is an urgent need for mass production using standardized manufacturing processes [15]. Standardized manufacturing offers several crucial benefits such as scalable precision manufacturing, comprehensive sealing capabilities to reduce environmental impact, and parametric tuning and optimization [16]. These factors play a vital role in optimizing the TENG output. However, the adoption of modern technologies is hindered by the challenges associated with the production of electrodes and thin films. Thin triboelectric films, typically ranging in thickness from a few micrometers, are essential for enabling electrostatic induction in most operating modes [2]. Unfortunately, many industrial manufacturing techniques, such as 3D printing, computerized numerical control (CNC) machining, micro-electro-mechanical systems (MEMS), and traditional machining, struggle to integrate films of such thinness into devices.

Fortunately, the freestanding (and rolling) mode of the TENG, known for its exceptional output compared to other modes, can operate effectively without relying on thin films. This characteristic opens up the potential for the TENG to be integrated into truly three-dimensional structures using a variety of industrial manufacturing techniques. Numerous researchers have been actively investigating the potential of employing various easy manufacturing techniques and approaches to develop 3D structures in this unique mode [17–20]. Notably, Yang et al.'s work on microbead-based TENG for ocean water energy harvesting has drew significant attention [19]. Their smart design involves coupling factory-manufactured microbeads (as negative triboelectric materials) with interlocking PCBs (serving as electrodes and supporting casings). This design offers several advantages, including standardization, low friction, truly 3D structure, and thus high spatial induction surface area efficiency. However, there is still room for improvement as the manual welding of PCB for electrical connectivity remains a challenge. Considering smart manufacturing as well, other researchers have explored microbeads TENG with 3D printing. However, most of these studies utilize 3D printing solely for casings and support components, with electrodes manually added through the use of adhesives, introducing varying degrees of low-precision human labor

Please cite this article in press as: L.N.Y. Cao et al., Materials Today (2023), https://doi.org/10.1016/j.mattod.2023.11.001

and reducing the device integration significantly [15]. Thus, there is a pressing need for pioneering advancements in parametric design, encapsulation, and standardized production processes for TENGs.

In this study, we propose a novel approach using the widely available fused deposition modeling (FDM) printer [18] with conductive (as electrodes) and nonconductive (as casing and supporting) filaments to encapsulate micro beads, creating a fully enclosed MB-TENG energy pack. This energy pack is then integrated with a wind-induced oscillator, enabling the harvesting of omnidirectional wind energy. On one hand, the modular TENG packs themselves, acting as an alternator array, can convert mechanical vibration energy (such as wind, ocean waves, and human motion) into AC power. These packs are fabricated using 3D printing technology in a print-in-place and post-processing-free manner, resulting in a one-piece, freestanding mode TENG with factory-made micro beads pre-encapsulated in multi-channels, allowing for impactful device systematic investigation and parametric optimization, and reaching the surface charge density as high as 19.9 $\mu C/m^2$ and peak output at 24.1 W/m^3. The calculation procedure of volumetric power density is given in Note S1 (Supporting information). Furthermore, this low-cost, streamlined process, with pre-encapsulation, allows for scalable and standardized mass manufacturing, easy coating for various resistance requirements, and widespread accessibility.

On the other hand, the wind oscillator serves as the energy converter, transforming kinetic energy from the wind into cyclic vibrational energy, which is then fed to the alternators, the energy packs [21,22]. This vibration-based mechanism reduces the impact on the environment, such as noise pollution, bird collisions, and falling hazards from conventional rotating blades, offering a flexible and eco-friendly approach to wind energy generation. When combined with the alternator and converter, this integrated system enables quiet and safe wind energy harvesting across various scales. In addition, the generated energy can power sensors that continuously collect environmental information, such as humidity and temperature, allowing for automatic and self-powered collection of valuable environmental data, which can be updated to the cloud and mobile terminals, and providing a solution to establish a data network for scientific data collection and location security with timely and efficient delivery of information.

Results and discussion

Structural design and application prospects of the energy harvesting system

Our wind energy harvesting system consists of the TENG energy pack as the energy alternator and the wind oscillator as the energy converter. The modular TENG packs were fabricated by 3D printing technology in a print-in-place manner with pre-encapsulated micro beads (Fig. 1a) and the detailed structure and working mechanism are presented in section 2.2. A 60 beads pack, which takes only 1 h to print and requires no post-processing, can immediately generate around 150 V. Thus, the energy pack with appropriate geometry can also function as converter to harvest unpredictable mechanical vibration energy with

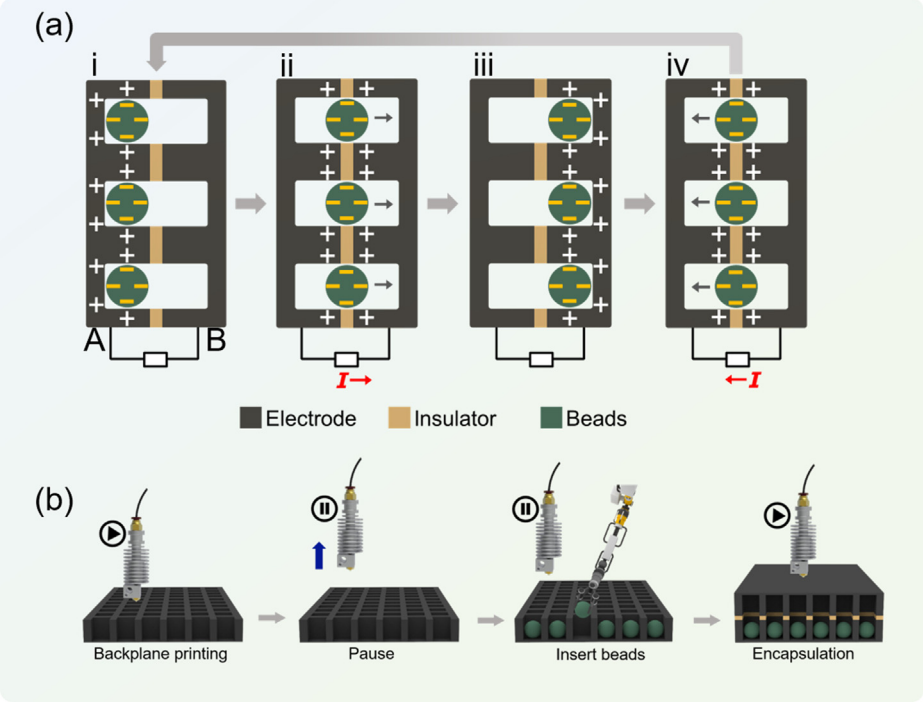

FIG. 2

Working schematic diagram and print flow chart of the energy pack. (a) The working principle of MB-TENG energy pack. (b) The preparation process of 3D printing of energy pack.

Please cite this article in press as: L.N.Y. Cao et al., Materials Today (2023), https://doi.org/10.1016/j.mattod.2023.11.001

a high degree of entropy, such as ocean waves and human motion (Fig. 1b).

The charge density is an important index to measure the electrical output performance of TENG. The use of PTFE beads as dielectric materials has been reported for a long time, and the surface charge density and bulk charge density are also very different due to the different structures. Therefore, we compared our work with the surface and bulk charge density (Table S1), and the manufacturing easiness in the literatures reported so far. Due to our parametric design and systematic optimization (described in section 2.4), our surface and volume charge density are as high as 19.9 $\mu C/m^2$ and 29856.5 $\mu C/m^3$ (Fig. 1c), respectively, which are much higher than other reported works [19,23–29]. More importantly, to our knowledge, the manufacturing technique of our approach stands out as the most dominant and superior.

With the excellent performance of the TENG energy pack, it is integrated with the wind oscillator as a portable system (also scalable) to convert wind energy into electrical energy. With a Y-shaped bluff body (Fig. 1d), our designed omnidirectional wind energy harvesting system can harvest wind energy in all direction. The specific fabrication progress can be found in the experimental section. The system, safer and quieter in comparison to traditional wind turbines, is suitable for operation in remote areas or near homes (Fig. 1e). The harnessed energy can be utilized to power IoT sensor networks, enabling the continuous and prolonged update of crucial environmental data to cloud and mobile platforms, thus establishing a smart monitoring system.

Working mechanism and design of TENG energy pack

The microbeads triboelectric nanogenerator (TENG) operates in a freestanding (or rolling) mode, with triboelectric components moving between two stationary electrodes. The working principle of the TENG energy pack is shown in Fig. 2a. In our design, the conductive carbon-filled polylactic acid (PLA) casing serves as both the electrodes (A and B) and the positive triboelectric components. The non-conductive PLA layer provides separation and insulation between them, while micro beads, with preferably negative charges, freely move within the conductive tunnels that surround them closely. When the device is agitated by external mechanical excitation (such as wind and water wave), charges will preferably transfer from the electrodes to the microbeads due to triboelectric effect [30,31] and alternating electric current will be generated between two electrodes due to electrostatic induction governed by Maxwell displacement current [2]. Therefore, the mechanical energy that drives the beads is converted into electrical energy.

Here we describe the charge transfer and current generation in detail. Due to the triboelectric effect, charge transfer occurs between the beads and electrodes. As the beads move along the tunnel surface, the molecules of different materials come into close proximity. This proximity causes the electron clouds of polytetrafluoroethylene (PTFE) and PLA materials to overlap [32], resulting in electron transfer following a specific sequence of negativity [30]. Electrostatic induction generates electric current from the transferred charges. In Step 1 of Fig. 2a(i) and 2a (ii), as the beads move from electrode A to B, the electrical potential on A decreases while the potential on B increases due to the arrival and departure of the negatively charged beads, respectively. Similarly, when the beads move from electrode B to A, the potential on B decreases and the potential on A increases due to the arrival and departure of negatively charged beads. Thus, the continuous generation of alternating current (AC) occurs as the beads oscillate within the tunnels.

To enhance the versatility and affordability of the design and manufacturing process, the TENG device has been specifically tailored to be compatible with widely available single-head FDM 3D printers (Fig. 2b). The design follows a sandwich structure, consisting of a conductive part, an insulating part, and another conductive part. During the printing process, a slight pause allows for the manual insertion of factory-made PTFE beads into the designated multi-channels, where each bead is encapsulated in its own channel to maximize the output (discussed in section 2.4). Subsequently, the printing continues, and the entire TENG device is sealed and fully enclosed by the printed conductive layer during the process. The detailed printing procedure is described in the Method section. Once the printing is completed, the TENG device is ready for immediate use, eliminating the need for any post-processing steps. This approach ensures that the device can be efficiently manufactured and put into operation without additional complexities.

Advantages of the design and manufacturing of the energy pack

3D printing enables parametric design and parameter optimization, allowing for easy adjustments to the inner and outer structures. This versatility allows for systematic comparisons of different inner parameters and the customization of the outer structure to suit specific applications, e.g., ocean wave harvesting [33]. The design is specifically tailored for manufacturing using a regular one-extruder FDM 3D printer, which is affordable and accessible, with prices as low as several hundred US dollars. Moreover, the use of commercially available conductive PLA filament ensures biodegradability [34]. By minimizing human interference during the printing process and eliminating post-processing, human labor is reduced and manufacturing errors are eliminated, resulting in consistent and reproducible device production. This approach enables on-demand, on-site production with controlled quality, low cost, and manufacturing flexibility.

Another notable advantage is the immediate full enclosure of the device upon printing. This enclosure provides effective protection against environmental factors, such as humidity, by minimizing air and liquid infiltration. With no critical moving parts inside the enclosure, the device exhibits increased lifetime and robustness. Furthermore, the enclosure facilitates easy coating of the device to enhance its resistance properties using techniques like dipping, painting, or spraying. Inside this enclosure, spherical beads employing rolling friction are utilized, enabling efficient harvesting of low-frequency and random vibration energy sources, including breeze wind, ocean waves, and human motions. The fully enclosed design, combined with streamlined industrial manufacturing processes, positions it as a commercially scalable product with diverse applications.

Please cite this article in press as: L.N.Y. Cao et al., Materials Today (2023), https://doi.org/10.1016/j.mattod.2023.11.001

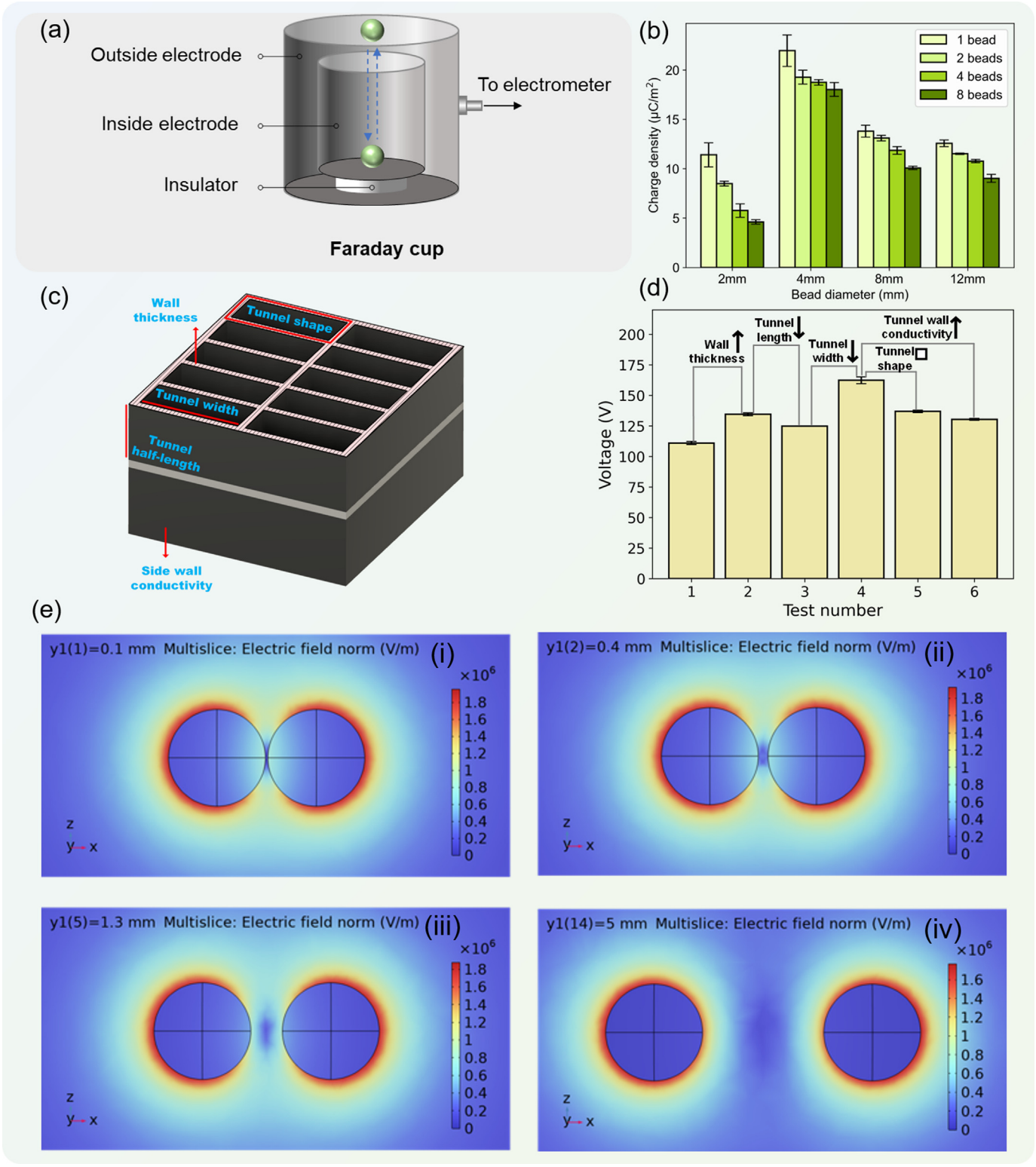

FIG. 3

Electrification performance of PTFE beads. (a) Schematic diagram of Faraday cup. (b) The surface charge density of PTFE beads in different diameters, measured by the Faraday cup method. (c) Cut-out view of the inner structures for the energy packs with investigated parameters. The top layer is cut off for visualization. (d) The total generated voltage of the energy pack containing 60 beads with different inner structures (the same group of beads). The favorable parameters are also indicated. (e) Simulated electric potential distribution between two beads with the same polarity charges by COMSOL software.

Bead characterization and TENG inner structure optimization

To optimize the TENG device, it is crucial to understand the factors that influence its output. The key aspects to consider are the final transferred charge between the positive and negative triboelectric materials and the electrical induction process. The transferred charge relies on the relative ability of the materials to

Please cite this article in press as: L.N.Y. Cao et al., Materials Today (2023), https://doi.org/10.1016/j.mattod.2023.11.001

acquire and donate electrons, while the induction is influenced by the charges and effective induction area, which is closely related to the structure of the induction area [14].

The charge characteristics primarily depend on the chosen materials. Although micro bead-based TENGs have been extensively studied, there has been a lack of investigation and evaluation regarding the surface charge density of the beads prior to their use. This absence of data makes it challenging to compare and optimize devices across studies, and simulation values may deviate significantly as well. Additionally, the inner structures around the beads have not been systematically explored due to the complexities and limited flexibility of existing manufacturing techniques. Therefore, it is necessary to establish a standardized method for characterizing both the beads and the inner structure.

Table S1 summarizes data from various studies that have utilized beads with different diameters (ranging from 4 to 18 mm) under diverse conditions. We have included normalized induced surface (from 6.6 to 19.9 $\mu C/m^2$) and volume charge density (from 3.1 to 29.8 mC/m^3) for comparative analysis. The widely used surface charge density is valuable for assessing the charge status of the beads, facilitating study comparisons and aiding in bead selection; the volume charge density becomes relevant when considering practical applications, device footprint, and the effectiveness of the device on a volume or mass scale. For example, data for references 1 and 3 in Table S1 show high surface charge density, but medium volume charge density, indicating less efficient devices on the volume scale. This is probably due to the use of relatively large beads, which results in less efficient usage of total surface area for electrostatic induction than small beads.

Micro beads characterization

Directly measuring the spatial charge distribution on a dielectric material with arbitrary shapes has proven to be challenging. However, an effective method for measuring particle charges is using the Faraday cup, commonly employed for measuring charges of particles in the air or charged droplets [35–37]. Since the charge carried by the materials is equal to the induced charges [36], we employed this method to indirectly measure the charges of the beads by quantifying the induced charges. The obtained results represent the induced charge amount over the entire surface area of the beads, referred to as effective surface charge density.

According to the bead diameter range summarized in Table S1, we selected PTFE beads with diameters of 2, 4, 8, and 10 mm for testing. We measured 1, 2, 4, and 8 beads, suspecting that the electric fields from multiple beads might partially cancel each other out. Our test device is a barrel-shaped Faraday cup, as shown in Fig. 3a. The charge on the bead's surface induces charge and voltage in the Faraday cup, which is capable of measuring the induced quantities. Each scenario was repeated three times. Fig. 3b illustrates the normalized charge density, calculated by dividing the measured charge by the total surface area of the beads for each diameter. In general, the 4 mm beads exhibit the highest charge density. However, the reason behind the superior performance of the 4 mm beads remains uncertain. It could be attributed to manufacturing factors, charging mechanisms, geometric influences on induction, or simply the dimensions of the beads in relation to the electric field. Additionally, as we hypothesized, the number of beads does impact the induced charges, with the density decreasing as the number of beads increases. This effect is likely due to the cancellation of electric fields between adjacent beads, which occurs both in standard testing and practical device applications. In our tests, we addressed this cancellation issue by implementing individual channels for each bead (an improvement from Case 1 to 2), as discussed in Section 2.4.2a.

Structural parameters

When the materials are determined, several structural parameters can significantly affect the overall output of the device. The discussion of these parameters is scattered in different studies, and each study tends to use its own metrics, making it challenging to compare results or conduct a systematic investigation. Fortunately, with the advent of 3D printing, we now have the freedom to explore and manipulate these parameters more effectively. We have designed and conducted a systematic comparison using a controlled variable method, where we vary one parameter at a time, generally ranging from the least to the most favorable. This approach allows us to clearly assess the impact of each parameter, which has not been done comprehensively in previous studies to our knowledge.

The structural parameters we investigate include the (1) wall thickness between tunnels, (2) tunnel length, (3) tunnel width, (4) tunnel shape, and (5) tunnel wall conductivity, illustrated in Fig. 3c. The summarized output results of 6 cases with various parameters can be found in Fig. 3d and the more detailed information is listed in Table S2. To quantitatively evaluate the effects, we normalize the voltage by the number of beads. Throughout the testing of structural parameters, we made efforts to maintain consistent testing conditions for all experiments. Each pack was designed to accommodate 60 beads (occupy almost half of the device inner volume) to eliminate any potential impact of bead number variation, although it should not significantly affect the results. We ensured that the same 60 beads were used in all tests to avoid any differences in bead charge density. Similar to the Faraday cup test, the beads were adequately charged for 30 min prior to the experiments.

a) Wall thickness (Case 1 vs 2): Based on the findings from the Faraday cup measurements, we concluded that the electric fields of adjacent beads cancel out each other. Therefore, we hypothesized that the layer thickness could also impact the output. We observed that a layer thickness of 1 mm resulted in a voltage per bead of 2.28 V, which was 21 % higher than the voltage per bead of 0.48 mm (1.88 V). When the wall thickness of adjacent channels is sufficiently thin, the electrical fields of beads in different channels (with the same polarity) can cancel each other out, reducing the electrical induction and overall output. Our simplified 3D numerical simulations confirmed a low electric field zone between closely spaced beads with the same polarity charges, resulting in reduced induction when an induction material is present (Fig. 3e). Interestingly, a recent study conducted by our group, using a similar simulation setup, demonstrated a strong electric field up to 10^9 V/m between conductive droplets carrying charges of opposite polarity, as

Please cite this article in press as: L.N.Y. Cao et al., Materials Today (2023), https://doi.org/10.1016/j.mattod.2023.11.001

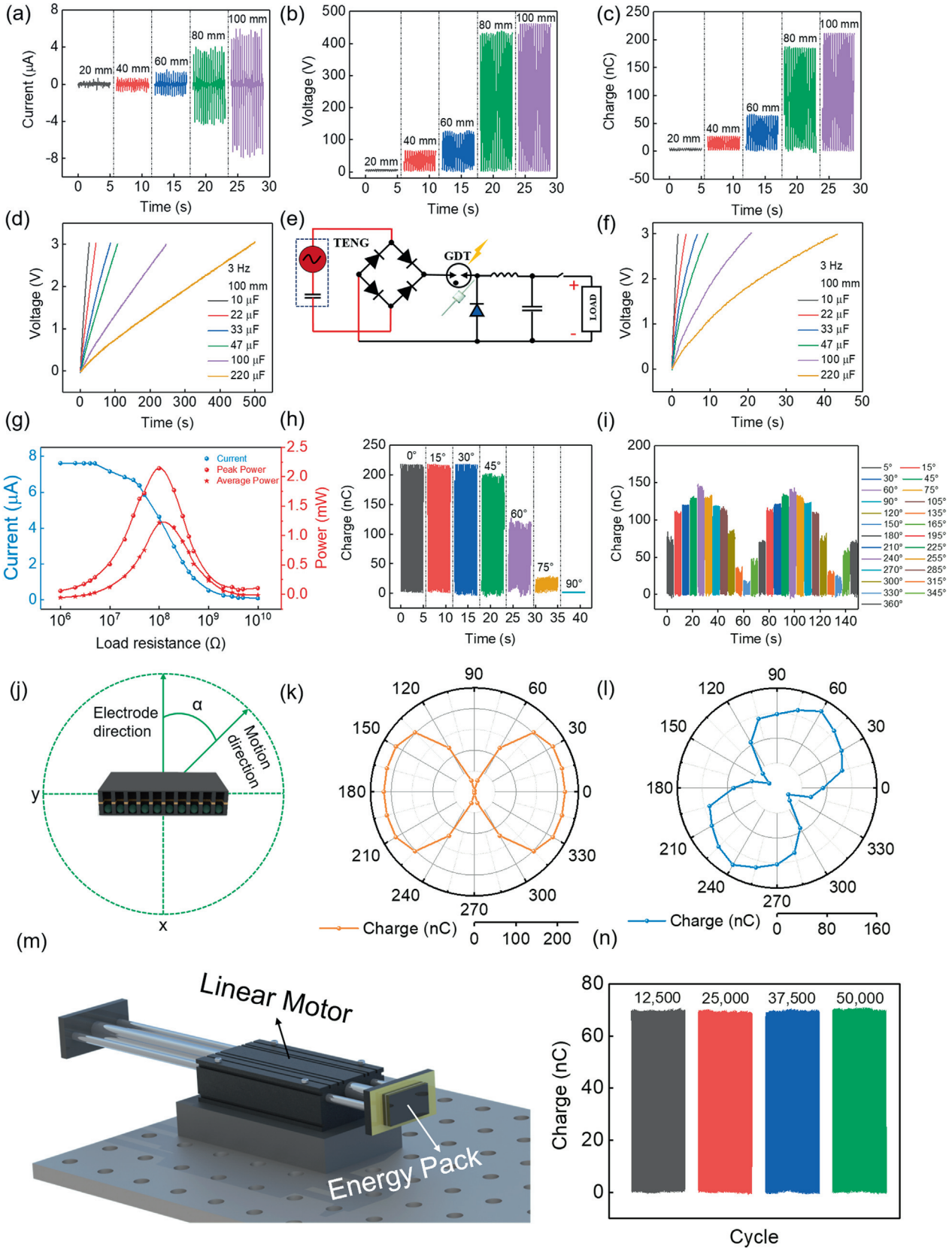

FIG. 4

TENG's electrical performance on the motor. (a) Different amplitudes of short-circuit current (b) Open-circuit voltage, and (c) transfer charge in the case of three TENGs hybrid of 3 Hz frequency with various stroke lengths. (d) Charge curves of different capacitors without any circuit connection. (e) The schematic diagram of the energy management circuit used. (f) The charging characteristic curve after the circuit is connected. (g) Peak power and average power of three TENG hybrids. (h) The angle dependence of the charge transfer of the three TENG mixtures. (i)The change of parallel transfer charge of three TENG with angle. (j) A schematic diagram of the α angle between the electrode direction and the swinging direction. (k) The fitting diagram of the change of the transferred charge with the angle of three TENG. (l) The fitting diagram of the change of parallel transfer charge of three TENG with angle. (m) Schematic diagram of linear motor testing. (n) 50,000 cycle charge durability test.

Please cite this article in press as: L.N.Y. Cao et al., Materials Today (2023), https://doi.org/10.1016/j.mattod.2023.11.001

opposed to charges of the same polarity, possibly facilitating spontaneous chemical reactions [38].

b) Tunnel length (Case 2 vs 3): Due to manufacturing difficulties, many designs in previous studies have multiple rows and columns of beads in a large tunnel, which limits the maximization of output. Although the voltage is similar between Case 2 and Case 3, it is important to note that the minimum stroke distance in Case 3 is proportional to the tunnel length. This increased tunnel length leads to a higher threshold travel distance, which hampers practical applications. Additionally, the current is reduced as the cycle length (for the bottom bead to pass the insulative layer) increases. However, considering the manufacturing challenges associated with devices featuring conductive tunnel walls, it is common to place multiple beads in a tunnel [19,29]. Fortunately, in our case, the manufacturing difficulty using 3D printing does not increase with the number and length of tunnels. This design with minimal tunnel length also offers minimum device thickness, making the device highly modular and flexible to various occasions, especially with limited size and space requirements.

c) Tunnel width (Case 3 vs 4): As observed in the comparison between Cases 1 and 2 and the Faraday cup experiments, when beads are too close to each other, they cancel out the electric field. Intuitively, if the number of beads is fixed, more channels would mean more induction surface area and higher output. This intuition is supported by the results shown in Fig. 3d that Case 4 with 2.76 V per bead (the highest among all cases) is 31 % higher than Case 3.

d) Tunnel shape (Case 4 vs 5): Complex tunnel shapes are extremely difficult to achieve using traditional techniques. In our study, we experimented with both square and circular tunnels. Intuitively, circular tunnels should create more effective induced surface areas. Surprisingly, our experimental results showed 21 % higher output using square tunnels compared to circular tunnels. The reason could be the bead will always cline to the corner of the square while only lay on part of the circular surface, giving more induction surface for square tunnel.

e) Tunnel wall conductivity (Case 4 vs 6): Previous studies exploring the use of conductive tunnel walls to maximize output have been limited due to challenging fabrication processes. Manual work has been involved in these few existing cases, while others have used single tunnels that do not maximize output. These limitations stem from the lack of an industrial-level approach for precision manufacturing. In contrast, our solution, utilizing 3D printed conductive channels in complex geometries, represents a significant advancement. Compared to other cases, the inclusion of a conductive tunnel wall in our design increases output significantly by 25 %.

In summary, a thorough examination of the device's internal structures reveals that the maximum output is produced by Case 4. This configuration confines every bead within its own tunnel featuring a square cross-section. The tunnel's half-length is equivalent to the bead's diameter, and the side-walls are conductive but cannot be too thin. In addition to ideal optimal output, the one-bead-one-channel feature can also prevent multiple beads from being in a single tunnel and may drastically reduce synchronization issues during irregular device movement in practical applications. Given these sophisticated parameters, 3D printing emerges as the most effective method for fabricating the device in a customized and standardized way, offering significant potential for large-scale production.

Electrical properties of TENG on bench test

TENG performance under different frequencies and stroke distances

In this section, we present experimental results evaluating the electric output of our generator device (Case 4 in Fig. 3d) under various operating conditions. The devices were subjected to varying frequencies and stroke lengths, and the measurements included current, voltage, and transferred charges. The excitation frequency and stroke length were systematically varied to explore their influence on the device's output (test diagram in Fig. S1). Three TENGs in hybrid were tested on the linear motor. We controlled the frequency of the linear motor to be 3 Hz, and the vibration amplitude gradually increased from 20 mm to 100 mm, as shown in Fig. 4 (a-c), the output of TENG gradually increases with the increase of amplitude. The experiment found that as the stroke length increases, the output gradually increases. Determined by the motor setting, an increase in the stroke length at the same shaking frequency results in an increase in shaking acceleration, which can provide more force and thus shorter distance of electrostatic induction when beads contact and leave the wall, thereby increasing the output. When the swing amplitude is 100 mm, the short-circuit current I_{sc} can reach 6 μA, and the open-circuit voltage V_{oc} is 461 V. A peak output of 212 nC of transferred charge can be achieved under the conditions of L = 100 mm and f = 3 Hz, which is much larger than that of previously reported devices with spherical shell structures (more than 7 times the charge output) [26], and the output It can be obtained without any amplification circuit. Detailed electrical output of single and three devices at different frequencies and amplitudes were shown in Fig. S2. Under the condition of frequency 3 Hz and amplitude 100 mm, the device has better electrical output performance. In general, the results show an increasing output with increasing stroke lengths and vibration frequencies (as high as 6 μA, 461 V, and 212 nC).

Charging test and power characteristic

An electric charging test was conducted to explore the generator unit's ideal capabilities. Fig. 4d shows three parallel TENG devices charging curves of capacitors with various capacities when charging a 220 μF capacitor. The 3 V threshold is reached in 500 s, too slow for powering the sensor. Thus, a matching full-wave rectification circuit (Fig. 4e) was designed to increase the charge rate. Rectification enables continuous capacitor charging and discharging via the gas discharge tube (GDT), achieving rapid charging.

Using a power management system (PMS) system, the unit efficiently charged a 220 μF capacitor to 3 V in under 1 min, achieving a 10-fold increase in charging speed (Fig. 4f). The specific parameters of the designed PMS can refer to the support material Note S2. This demonstrates the unit's effectiveness in harnessing energy and efficiently charging circuits. It showcases its potential for powering various electronic devices and systems through efficient energy conversion and storage.

The relationship between the optimal output (including peak current I_{peak}, peak power P_{peak} and average power P_{ave}) and resis-

Please cite this article in press as: L.N.Y. Cao et al., Materials Today (2023), https://doi.org/10.1016/j.mattod.2023.11.001

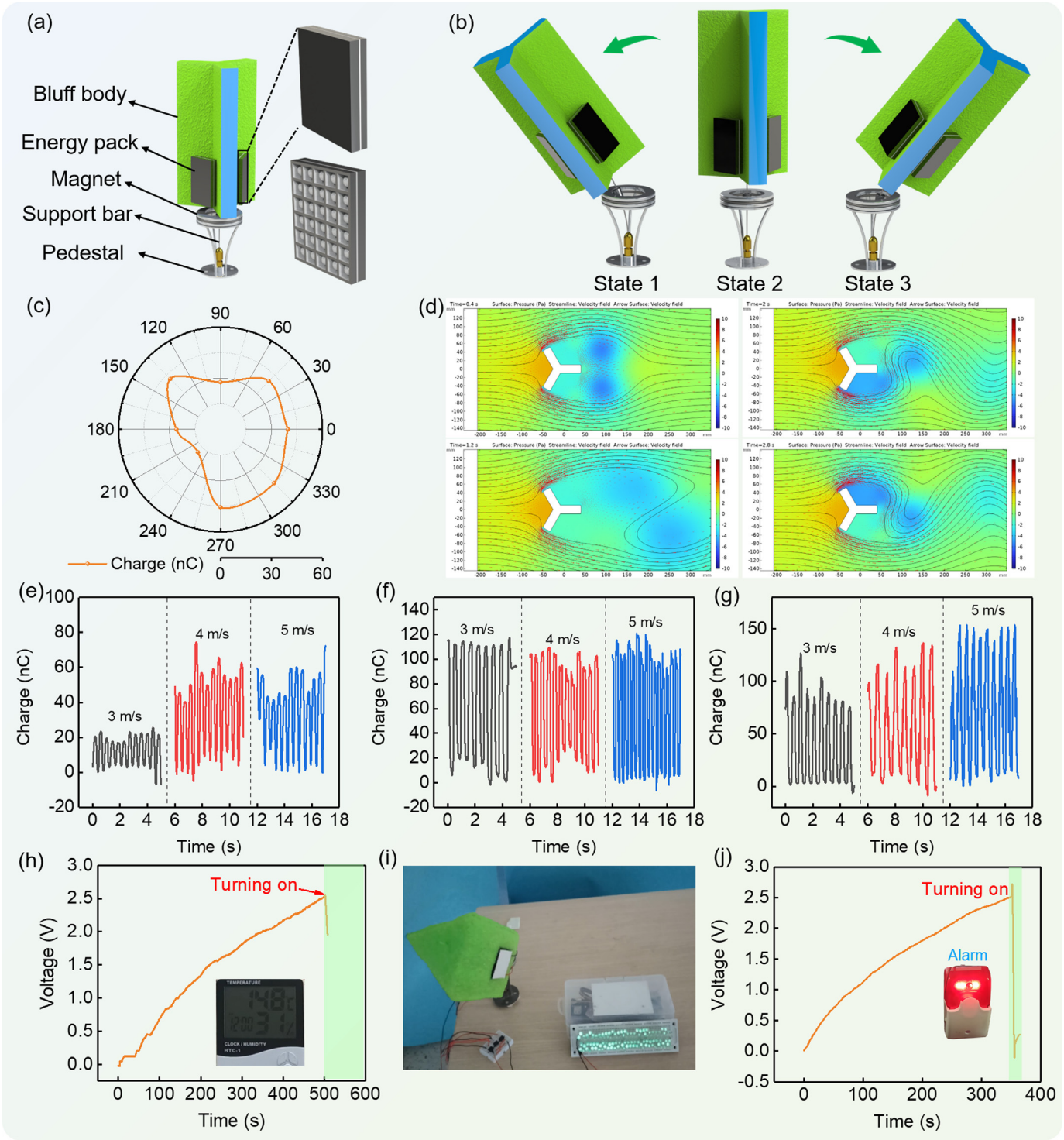

FIG. 5

Output performance under the condition of wind field. (a) Schematic diagram of the MB-TENG installation. The illustration is an enlarged picture of TENG and the distribution of internal pellets. (b) A schematic diagram of the working state of MB-TENG. (c) The fitting diagram of Y-shaped transfer charge varying with the angle. (d) The flow and pressure fields with the bluff body are simulated by COMSOL Multiphysics software using finite element method. (e) Comparison of output of square bluff body, (f) triangular bluff body and (g) Y-shaped bluff body at different wind speeds. (h) The voltage curve of the thermohygrometer driven by a square bluff body. (i) The triangular bluff body lights 120 LED lamps in series at the same time in the swinging state. (j) The voltage curve of the Y-shaped bluff body drive alarm.

Please cite this article in press as: L.N.Y. Cao et al., Materials Today (2023), https://doi.org/10.1016/j.mattod.2023.11.001

tive loads R is shown in Fig. 4g. The average power is calculated by the following formula

$$P_{ave} = \frac{\int_0^T I(t)^2 R dt}{T} \quad (1)$$

where T is the output period and I is the output current. Under linear shaking at 3 Hz, the maximum peak power is 2.1 mW, the maximum average power is 1.2 mW, and the matching impedance is about 100 MΩ.

TENG performance under various numbers of packs and different installation angles

In order to demonstrate the scalability of the modular energy packs, we conducted an experiment where we connected all A and all B electrodes of 1,2,3 packs (mixed-connection), and then measured the output. This approach allowed us to establish a linear relationship, indicating significant scalability for the energy packs (Fig. S3). These packs are designed to accommodate varying numbers of beads and can be manufactured either as a single piece or by externally connecting modular packs. To illustrate this, we parallel connected packs with 60 beads across 1 to 3 modules. The normalized voltage displayed minimal variation, while the total output exhibited a consistent linear relationship with the number of beads. This demonstrates that the pack's performance is directly proportional to the number of beads and can be easily scaled up with flexibility.

The direction of external excitation is not always along the direction of the tunnel (i.e. the direction of the electrodes). There is usually an angle between them. As shown in Fig. 4j, α is defined as the angle between the external excitation direction and the electrode direction. With the change of angle α, the output performance of MB-TENG will also change significantly. For the output of multiple MB-TENG devices, different connection methods have different output characteristics. Based on this, we designed two connection methods, hybrid connection and parallel connection, their connection circuit schematic diagram is shown in Fig. S4.

The angle between the device motion direction and the beads moving direction may affect the output, especially for the real-world applications. Thus, we evaluated the performance of the unit comprising three devices and examined the impact of angle on its electric output (Fig. S5a). In a mix-connection state, the unit demonstrated the highest output when positioned at an angle of 0 degree (Fig. 4h and 4 k). The output gradually decreased as the angle deviated from the optimal position and starts to rise again and reaches saturation at 180° (Fig. 4k). The variation curve of the corresponding current with the angle is shown in Fig. S5. Then we connected three packs with rectifier (parallel connection) to test the total output every 15 degree (Fig. S5b). Fig. 4i and 4 l shows the rectified output under different shaking directions in the same frequency. There are preferable directions, but omnidirectional feasibility is approved (current from around 20 to 150 μA). These findings underscore the significance of angle adjustment for maximizing the unit's energy harvesting efficiency and help the arrangement of packs in the array for real-world omnidirectional applications. In addition, in order to explore the stability of the energy package after working for a long time, we used the motor shown in Fig. 4m to conduct a 50,000-cycle test for 5 h, and the output stayed stable (Fig. 4n). This shows that the device has the potential to maintain long-term stability in practical applications.

Design and optimize the wind-induced oscillator

To allow omnidirectional wind harvesting, a wind oscillator was specifically developed. Unlike wind vanes commonly used for environmental monitoring, which require a minimum wind speed to rotate and experience energy loss during turning, our wind oscillator for omnidirectional wind harvesting overcomes these limitations. It eliminates the need for rotational mechanisms and moving parts like gears, avoiding wear and tear issues and providing a more efficient and reliable solution.

Wind-induced oscillating mechanism

The wind energy system design features a stand made of metal 3D-printed aluminum, firmly holding a carbon fiber rod with a clamp (Fig. 5a). A ring magnet is fixed on the stand, while smaller magnets with opposite polarity are attached to the rod. The rod supports a lightweight foam prism serving as the mast, with three TENG packs embedded on its horizontal surfaces.

The wind-induced oscillator operates through the aerodynamic force generated by the passing wind. This aerodynamic phenomenon, known as galloping, is a one-degree-of-freedom instability characterized by a velocity-dependent, damping-controlled oscillation at a low frequency (approximately 1 Hz) with high amplitude. These galloping oscillations are ideal for energy harvesting, yielding significant output. Galloping commonly occurs in non-streamlined structures like squares, rectangles, and triangles [39–42] . Certain shapes exhibit wind forces and instantaneous vibration directions (perpendicular to the wind direction) that align in the same direction. This synchronization results in cyclic motion and consistent energy output. The bluff body with a square cross-section is susceptible to vibrations caused by wind from all directions, making it an omnidirectional energy harvesting solution.

The carbon fiber rod serves a dual purpose in the system: enabling wind-induced vibrations for energy generation and providing vertical support. However, a challenge arises as the rod needs to be flexible yet stiff enough to support the system. To address this, reinforcement magnet rings are introduced to enhance support and enhance oscillation and damping effects. The magnetic force between these permanent magnets follows an inverse square relationship with the average distance between their poles, creating a spring-like behavior with non-constant elasticity based on displacement. These magnets limit the maximum amplitude, fine-tune the frequency, and prevent overreaching of the mast, allowing for precise amplitude control without interfering under low-amplitude conditions.

With the simplification of load at a given point for a cantilever round beam, the maximum deflection can be calculated by the following equation:

$$\delta_{max} = \frac{Pa^2(3L - a)}{6EI} \quad (2)$$

where P is the load force from the wind, a is the load point to the pivot point, L is the length of the rod, E is the modulus of elastic-

Please cite this article in press as: L.N.Y. Cao et al., Materials Today (2023), https://doi.org/10.1016/j.mattod.2023.11.001

ity, and I is the moment of inertia. For rod with a circular cross, the moment of inertia can be calculated by

$$I = \frac{\pi r^4}{4} \tag{3}$$

where r is the rod radius.

With the added pair of magnet rings, the frequency of oscillation is expressed by

$$f(x) = \frac{1}{2\pi}\sqrt{\frac{(k + k'(x))}{m} - \left(\frac{c}{2m}\right)^2} \tag{4}$$

where k' represents the amount of elasticity corresponding to the magnetic repulsion. elasticity constant k and a damper of constant c.

We define the whole swing process as state 1, intermediate state 2, and state 3 (Fig. 5b). When the bluff body swings from intermediate state 2 to state 1, the support rod is subjected to the repulsive force of the magnet and the reverse force of the rebound to generate a reverse acceleration. Similarly, the three TENG unit elements also have a reverse acceleration, so that the internal PTFE beads start to contact and separate from the electrode at one end; similarly, when the bluff body swings from intermediate state 2 to state 3, the three TENG unit elements have a reverse acceleration, so that the inner PTFE beads start to contact the electrode at the other end. Contact separation occurs, and the cycle repeats to generate an alternating current signal. Accordingly, we show the force analysis of the carbon fiber rod in state 1 and state 3 in Fig. S6, which is subjected to both elastic and magnetic forces.

Effect of mast shapes

To assess the performance of energy packs on different mast shapes (triangle, square, and Y-shape), we conducted tests under simulated consistent wind speeds. In each experiment, three packs were mounted on individual masts, with only the highest-performing pack measured. To ensure unbiased wind conditions, a fan with a diameter significantly larger than the device was used to generate wind speeds ranging from 3 m/s up to 5 m/s. The results, shown in Fig. 5(e-g), revealed that the Y-shape bluff body demonstrated the highest output (150 nC). In addition, the current and voltage data plots of different bluff bodies under different wind speeds can be found in the supporting material Figs. S8-S10. A simplified 2D computational fluid dynamics (CFD) transient simulation by COMSOL Multiphysics was conducted to investigate the flow evolution and the oscillation mechanism of the Y-shaped mast (Fig. 5d, Video S1). As the wind at 3 m/s flows from the left to right, the flow direction and air pressure difference between upper and lower side of the mast switch sides over time (Fig. S6), causing the cyclic imbalanced force to oscillate the mast.

Effect of wind directions

Next, we proceeded to connect three packs, which were mounted on the Y-shaped mast, with a rectifier to assess the total output. In the practical wind field, the devices will face random wind direction due to the randomness of the wind. Therefore, we tested the output of the MB-TENG facing various wind directions. As shown in Fig. 5c, by continuously rotating the included angle of the chassis to adjust the windward side, it can be seen that the device is at 0°, 45°, 135°, 270°, and 315° have larger outputs, and this experiment proves that MB-TENG has the function of omnidirectional wind energy collection. The angle-dependent curves of triangular and Y-shaped currents can be found in Fig. S7. While certain wind directions proved to be more favorable, the overall feasibility of omnidirectional energy generation was confirmed.

Application of the wind oscillator

To demonstrate the potential of MB-TENG in wind energy harvesting, around the needs of various application environments, related application demonstrations were carried out under the action of a wind field of 5 m/s with various mast shapes (square, triangle, and Y-shape) to fit various potential scenarios: temperature and humidity meter monitoring, lighting of LED lights, and wireless alarm. Fig. 5h shows that MB-TENG can drive a commercial thermo-hygrometer (Video S2) after charging for 500 s, and the thermo-hygrometer works normally to obtain the local temperature and humidity conditions. As shown in Fig. 5i (Video S3), 120 LEDs lights with a diameter of 5 mm in series are lit simultaneously, which can be used as direction indicators for road signs. MB-TENG can be used as a fire warning power supply. As shown in Fig. 5j (Video S4), a 330 μF capacitor is charged to 2.5 V after 350 s. At this time, turning on the discharge switch can trigger a commercial wireless alarm transmitter to start working, separated by several meters. The remote alarm will start to send out harsh alarms after receiving the transmission signal, to remind the user that there are dangers or potential situations, such as early warnings such as fires and earthquakes. The device is also brought to natural wind for field measurement and device can consistently generate signals measured by the electrometer in a calm outdoor environment with periodic breeze (Fig. S11, Video S5). We characterized the surface of the PTFE beads before and after stability test with standard laboratory setup, and the results are shown in Figs. S12 and S13. After long-term stability testing, there were no major changes in the surface of the beads and walls. The charge density stays stable, demonstrating the long-term stability of the microbeads TENG. The laboratory and field results show that together with the battery-less monitoring, alarming, and wireless signal transmission, the system demonstrates substantial potential as a valuable resource for environmental monitoring and alerts.

Conclusions

To facilitate the transition of the emerging triboelectric nanogenerators (TENG) from early stages to large-scale real-world applications, we developed a novel 3D printing method to make fully enclosed microbeads structured TENG arrays (MB-TENG) including 3D printed electrodes. The process requires absolutely no postprocessing with a "pause-and-insert" and "print-in-place" manner, and devices can be used as generators right off any prevailing FDM printer. With the help of parametric design and streamlined manufacturing, we have systematically investigated the effect of the inner structure parameters (6 cases) on the device performance, and developed a Faraday cup method to investigate the charge density of microbeads, providing a universal reference and standardized method to design inner structures

Please cite this article in press as: L.N.Y. Cao et al., Materials Today (2023), https://doi.org/10.1016/j.mattod.2023.11.001

and characterize microbeads. The optimized device achieves the highest both surface and volume charge density of the beads, and the highest industrialization level among all microbeads studies.

In summary, the study provides a promising strategy towards parametric optimization, and large-scale standard and customized manufacturing of TENG energy packs. The versatile energy packs were integrated with a wind-induced galloping oscillator to harvest omnidirectional wind energy, forming a closed loop self-powered sensing system and offering power to run environmental IoT devices for, such as temperature, humidity, and atmospheric pressure. The novel Y-shape mast with a magnetic turning system offers high response to breeze with high system robustness. Beyond its wind energy application, the versatile energy packs can serve as both ocean wave and human motion harvesters within network configurations, capable of powering a massive real-time monitoring sensor array.

Experimental section

Printing process: The printing process starts by extruding the conductive material to form the bottom part with individual channels, which serves as the first conductive part of the sandwich structure. Once the first part is printed, the printer temporarily pauses its operation. During this pause, we manually insert small PTFE beads into the designated channels. After the PTFE beads are inserted, the printing process resumes. The printer adds an insulating layer on top of the first conductive part, ensuring proper separation between the conductive parts. The printer then extrudes the conductive material again to form the top part, completing the sandwich structure. As the printing progresses, the conductive layers fully encapsulate the PTFE beads, creating a sealed and enclosed TENG device. Once the printing is complete, the TENG device is allowed to cool and solidify. Any excess material or support structures are removed, leaving behind a fully functional TENG device. The detailed printing process described above combines precise layer-by-layer deposition with a manual insertion step to incorporate the triboelectric components. The resulting printed TENG device exhibits a well-sealed structure, ready for further testing and energy harvesting applications. The conductive carbon-filled PLA (polylactic acid) filament is purchased from Proto-pasta.com. The typical resistance of a 10 cm length of the 1.75 mm filament is 2.5–3.5 kohm.

Preparation of the omnidirectional wind energy collector: First, the designed base is prepared by 3D printing of stainless steel, and 4 M6 threaded holes are reserved at the bottom of the base for outdoor test fixing points. Then place two ring magnets with an outer diameter of 50 mm, an inner diameter of 25 mm, and a thickness of 5 mm on the top of the base. The inner diameter of the magnet is covered with two small ring magnets with an outer diameter of 10 mm, an inner diameter of 6 mm, and a thickness of 5 mm. And a carbon fiber rod with a length of 20 mm and a diameter of 1.3 mm passes through, and the bottom end of the carbon fiber rod is tightly fixed in the buckle at the bottom of the base. Finally, the Y-shaped foam glued with the TENG device is inserted into the carbon fiber rod and packaged and fixed. Among them, the Y-shaped foam has a length of 190 mm, a top view diameter of 110 mm, a blade width of 48.3 mm, a thickness of 20 mm, and an angle of 120° between the blades.

Electrical performance measurement and characteristics of the device: Wind is generated by a commercial floor fan (FS-750, DIAMOND, China), controlled by an AC speed controller (ZADY6000X, CHNK, China), and wind speed and direction are controlled by an integrated anemometer RS458 (LYA, LONGYUN SENSOR, China) test. The output signal of the device was measured by an electrometer (6514, Keithley, USA). The measurement is driven by a linear motor (LinMot E1100).

CRediT authorship contribution statement

Leo N.Y. Cao: Conceptualization, Methodology, Software, Data curation, Writing – original draft, Visualization, Investigation, Writing – review & editing. **Erming Su:** Visualization, Investigation, Formal analysis, Software, Writing – original draft, Writing – review & editing. **Zijie Xu:** Visualization, Investigation, Writing – review & editing. **Zhong Lin Wang:** Supervision, Conceptualization, Funding acquisition, Project administration, Resources, Writing – review & editing.

Data availability

Data will be made available on request.

Declaration of competing interest

The authors declare that they have no known competing financial interests or personal relationships that could have appeared to influence the work reported in this paper.

Acknowledgements

Support from the National Key R & D Project from Minister of Science and Technology (2021YFA1201601), National Natural Science Foundation of China (Grant No. 52192610), and CAS Youth Interdisciplinary Team are appreciated.

Appendix A. Supplementary data

Supplementary data to this article can be found online at https://doi.org/10.1016/j.mattod.2023.11.001.

References

[1] M. Majid et al., Sensors (Basel) 22 (6) (2022) 2087.
[2] C. Wu et al., Adv. Energy Mater. 9 (1) (2019) 1802906.
[3] A. Goldthau, S. Tagliapietra, Nature 612 (7941) (2022) 627–630.
[4] F.R. Fan et al., Nano Energy 1 (2) (2012) 328–334.
[5] D. Choi et al., ACS Nano 17 (12) (2023) 11087–11219.
[6] L.N.Y. Cao et al., Nanomaterials (Basel) 12 (19) (2022) 3261.
[7] Y. Luo et al., Adv. Funct. Mater. 32 (39) (2022) 2205710.
[8] E. Su et al., Adv. Funct. Mater. 13 (2023) 2214934.
[9] Z.-H. Lin et al., Adv. Mater. 26 (27) (2014) 4690–4696.
[10] Z.-H. Lin et al., Angew. Chem. Int. Ed. 52 (48) (2013) 12545–12549.
[11] S.A. Lone et al., Nano Energy 99 (2022) 107318.
[12] C. Yeh et al., Nano Energy 104 (2022) 107852.
[13] Z. Xu et al., Nat. Commun. 14 (1) (2023) 2792.
[14] J. Shao et al., Adv. Energy Mater. 11 (16) (2021) 2100065.
[15] G. Liu et al., EcoMat 3 (5) (2021) e12130.
[16] L. Zu et al., Sci. Adv. 9 (20) (2023) eadg5152.
[17] B.D. Chen et al., Nano Energy 45 (2018) 380–389.
[18] B.D. Chen et al., Mater. Today 50 (2021) 224–238.
[19] X. Yang et al., Nano Energy 60 (2019) 404–412.

Please cite this article in press as: L.N.Y. Cao et al., Materials Today (2023), https://doi.org/10.1016/j.mattod.2023.11.001

[20] Y. Duan et al., Nano Res. 16 (9) (2023) 11646–11652.
[21] R. Tandel et al., J. Phys. Conf. Ser. 1950 (1) (2021) 012058.
[22] D.Y. Villarreal, V.B. SL, Vortex Blade-less SL (2018).
[23] J. Chang et al., Nano Energy 98 (2022) 107271.
[24] Y. Pang et al., Nano Energy 66 (2019) 104131.
[25] X. Wang et al., Appl. Energy 323 (2022) 119648.
[26] X. Xiao et al., Adv. Energy Mater. 9 (40) (2019) 1902460.
[27] M. Xu et al., ACS Nano 13 (2) (2019) 1932–1939.
[28] S.L. Zhang et al., Nano Energy 48 (2018) 421–429.
[29] Z. Zhang et al., J. Mar. Sci. Eng. 10 (4) (2022) 455.
[30] H. Zou et al., Nat. Commun. 10 (1) (2019) 1427.
[31] Y. Xi et al., Nano Energy 38 (2017) 101–108.
[32] C. Xu et al., Adv. Mater. 30 (38) (2018) e1803968.
[33] S. Xu et al., Adv. Energy Mater. 12 (3) (2021) 2103408.
[34] L. Shao et al., Green Chem. 24 (22) (2022) 8716–8724.
[35] L.N.Y. Cao, D.Y.H. Pui, J. Aerosol Sci 117 (2018) 11–23.
[36] M. Kaponig et al., Sci. Adv. 7 (22) (2021) eabg7595.
[37] Z. Tang et al., Adv Mater 33 (42) (2021) e2102886.
[38] S. Lin, et al., 120(31) (2023) e2307977120.
[39] W. Wang et al., iScience 25 (11) (2022) 105374.
[40] M.P. Païdoussis et al., Fluid-structure Interactions: Cross-flow-induced Instabilities, Cambridge University Press, 2010.
[41] Y. Tian et al., Appl. Phys. Lett. 121 (9) (2022) 093902.
[42] F.-R. Liu et al., Appl. Phys. Lett. 112 (23) (2018) 233903.

Please cite this article in press as: L.N.Y. Cao et al., Materials Today (2023), https://doi.org/10.1016/j.mattod.2023.11.001